Bi2O2CO3 Growth at Room Temperature: In Situ X-ray Diffraction Monitoring and Thermal Behavior

Moré, René ; Olah, Michael ; Balaghi, S Esmael ; Jäker, Philipp ; Siol, Sebastian ; Zhou, Ying ; Patzke, Greta R

Abstract: The room-temperature formation of bismuth oxycarbonate (Bi2O2CO3) from Bi2O3 in sodium carbonate buffer was investigated with in situ powder X-ray diffraction (PXRD) in combination with electron microscopy and vibrational spectroscopy. Time-resolved PXRD measurements indicate a pronounced and rather complex pH dependence of the reaction mechanism. Bi2O2CO3 formation proceeds within a narrow window between pH 8 and 10 via different mechanisms. Although a zero-dimensional nucleation model prevails around pH 8, higher pH values induce a change toward a diffusion-controlled model, followed by a transition to regular nucleation kinetics. Ex situ synthetic and spectroscopic studies confirm these trends and demonstrate that in situ monitoring affords vital parameter information for the controlled fabrication of Bi2O2CO3 materials. Furthermore, the $\rightarrow$ bismuth oxide transformation temperatures of Bi2O2CO3 precursors obtained from different synthetic routes differ notably (by min 50 °C) from commercially available bismuth oxide. Parameter studies suggest a stabilizing role of surface carbonate ions in the as-synthesized bismuth oxide sources. Our results reveal the crucial role of multiple preparative history parameters, especially of pH value and source materials, for the controlled access to bismuth oxide-based catalysts and related functional compounds.

DOI: https://doi.org/10.1021/acsomega.7b01359

ACS OMEGA

Article

Cite This: ACS Omega 2017, 2, 8213-8221

http://pubs.acs.org/journal/acsodf

$Bi_2O_2CO_3$ Growth at Room Temperature: In Situ X-ray Diffraction Monitoring and Thermal Behavior

René Moré,[†,⊥] Michael Olah,[†,⊥] S. Esmael Balaghi,[†] Philipp Jäker,[‡] Sebastian Siol,[§] Ying Zhou,[∥] and Greta R. Patzke*[,†]

[†]Department of Chemistry, University of Zurich, Winterthurerstrasse 190, CH-8057 Zurich, Switzerland

[‡]Laboratory for Multifunctional Materials, Department of Materials, ETH Zurich, Vladimir-Prelog-Weg 5, CH-8093 Zurich, Switzerland

[§]Laboratory for Joining Technologies and Corrosion, Empa, Swiss Federal Laboratories for Materials Science and Technology, Überlandstrasse 129, CH-8600 Dübendorf, Switzerland

[∥]The Center of New Energy Materials and Technology, School of Materials Science and Engineering, Southwest Petroleum University, 610500 Chengdu, China

Supporting Information

ABSTRACT: The room-temperature formation of bismuth oxycarbonate ($Bi_2O_2CO_3$) from Bi_2O_3 in sodium carbonate buffer was investigated with in situ powder X-ray diffraction (PXRD) in combination with electron microscopy and vibrational spectroscopy. Time-resolved PXRD measurements indicate a pronounced and rather complex pH dependence of the reaction mechanism. $Bi_2O_2CO_3$ formation proceeds within a narrow window between pH 8 and 10 via different mechanisms. Although a zero-dimensional nucleation model prevails around pH 8, higher pH values induce a change toward a diffusion-controlled model, followed by a transition to regular nucleation kinetics. Ex situ synthetic and spectroscopic studies confirm these trends and demonstrate that in situ monitoring affords vital parameter information for the controlled fabrication of $Bi_2O_2CO_3$ materials. Furthermore, the $\beta \rightarrow \alpha$ bismuth oxide transformation temperatures of $Bi_2O_2CO_3$ precursors obtained from different synthetic routes differ notably (by min 50 °C) from commercially available bismuth oxide. Parameter studies suggest a stabilizing role of surface carbonate ions in the as-synthesized bismuth oxide sources. Our results reveal the crucial role of multiple preparative history parameters, especially of pH value and source materials, for the controlled access to bismuth oxide-based catalysts and related functional compounds.

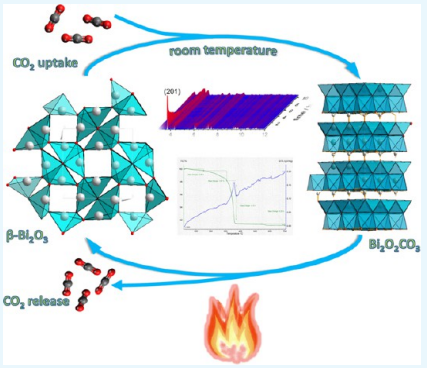

INTRODUCTION

The depletion of fossil fuel resources along with increasing worldwide climate and water pollution issues raises the urgent demand for low-cost photocatalytic materials for solar fuel production and water cleaning. Bismuth oxide-related materials have emerged as a growing family of attractive environmental research targets.[1] Among them, bismuth oxycarbonate ($Bi_2O_2CO_3$) keeps attracting interdisciplinary interest due to its manifold properties. They are linked to its Sillén-type layered structure consisting of $[Bi_2O_2]^{2+}$ layers interleaved by slabs comprising CO_3^{2-}.[2−9] $Bi_2O_2CO_3$ excels through high photocatalytic activity in waste water cleaning or NO_x removal,[2−6,8−16] and it furthermore exhibits a large nonlinear optical effect,[4,17] humidity sensing properties,[7] and antibacterial activity.[18]

Therefore, several synthetic routes to obtain $Bi_2O_2CO_3$ nanomaterials have been reported, and many of them are based on small organic molecules as CO_3^{2-} sources, such as urea[4,5,12,13] or citrate.[4,5,10,13−16] In comparison, we developed an economic and environmentally friendly room-temperature route to $Bi_2O_2CO_3$ using β-Bi_2O_3 as starting material. This route offers additional options for chemical CO_2 capture and storage.[7] The formation pathway of $Bi_2O_2CO_3$ nanosheets most likely proceeds via bismuth hydroxide $(BiO)_4(OH)_2CO_3$ as an intermediate species. CO_2 is dissolved in water and forms CO_3^{2-} that diffuses to the surface of Bi_2O_3, where a plausible reaction mechanism can take place via heterogeneous nucleation of $(BiO)_4(OH)_2CO_3$ and $Bi_2O_2CO_3$ (cf. eqs 1 and 2). In the final step, intermediate $(BiO)_4(OH)_2CO_3$ is transformed into $Bi_2O_2CO_3$ (eq 3)[7]

$$2Bi_2O_3(s) + CO_3^{2-} + 2H_2O \rightarrow (BiO)_4(OH)_2CO_3(s) + 2OH^- \quad (1)$$

$$Bi_2O_3(s) + CO_3^{2-} + H_2O \rightarrow Bi_2O_2CO_3(s) + 2OH^- \quad (2)$$

Received: September 13, 2017
Accepted: November 7, 2017
Published: November 20, 2017

DOI: 10.1021/acsomega.7b01359
ACS Omega 2017, 2, 8213−8221

$$(BiO)_4(OH)_2CO_3(s) + CO_3^{2-} \rightarrow 2Bi_2O_2CO_3(s) + 2OH^- \quad (3)$$

Generally, photocatalytically active materials show a strong influence of their morphology and crystallinity on the catalytic activity.[4,14,19,20] However, comparably little is still known about the role of these key parameters in $Bi_2O_2CO_3$ fabrication.[14] In an earlier study, higher activities for photocatalytic rhodamin B degradation and NO_x removal as well as higher photocurrents were observed for $Bi_2O_2CO_3$ with dominantly exposed {001} planes.[4] In contrast, remnant $(BiO)_4(OH)_2CO_3$ contents exerted a negative influence on the activity in photocatalytic NO_x removal.[13] This renders deeper insights into the formation and thermal decomposition processes of $Bi_2O_2CO_3$ essential for the optimization and targeted exploration of this multifunctional material.

Furthermore, the enhanced photocatalytic properties of $Bi_2O_3/Bi_2O_2CO_3$ heterojunctions are in the focus of recent research activities.[21−23] The majority of these composites were formed after several hours of thermal treatment of $Bi_2O_2CO_3$ in the range between 300 and 400 °C,[21−23] which gives rise to partial or full conversion into β-Bi_2O_3.[24] α-$Bi_2O_3/Bi_2O_2CO_3$ heterojunctions are less common in comparison, and only recently was their formation observed in the above temperature range, namely at 350 °C.[25] Generally, the reported temperature windows for the transformation sequence $Bi_2O_2CO_3 \rightarrow \beta$-$Bi_2O_3 \rightarrow \alpha$-$Bi_2O_3$ vary significantly between studies (cf. survey in Tables S1 and S2). This sheds interesting light on the particle size dependence of the β-$Bi_2O_3 \rightarrow \alpha$-$Bi_2O_3$ phase transition that was first mentioned several decades ago[26] and remains a subject of current studies, which also revealed the influence of surface carbonate formation on the phase stability.[27] Further investigations are thus required to establish reliable fabrication conditions for specific heterojunction types.

In situ diffraction studies are perfectly suited for growth-dependent parameter studies because they permit a most direct monitoring of nanomaterial formation processes.[28−34] Therefore, we applied time-resolved powder X-ray diffraction (PXRD) to acquire detailed insight into the reaction mechanism involved in the room-temperature formation of $Bi_2O_2CO_3$. Special emphasis was placed on the impact of the molecular environment, namely pH value and CO_2 partial pressure, on the formation pathways of $Bi_2O_2CO_3$ nanoparticles. Moreover, we demonstrate that the choice of starting materials and the preparative history exert a significant effect on the $Bi_2O_2CO_3 \rightarrow \beta$-$Bi_2O_3 \rightarrow \alpha$-$Bi_2O_3$ transition sequence.

RESULTS AND DISCUSSION

In Situ PXRD Monitoring of $Bi_2O_2CO_3$ Formation. pH-Dependent three-dimensional stack plots of in situ PXRD patterns monitoring the formation of bismuth oxycarbonate at room temperature are shown in Figure 1. The Bragg reflections of the initial PXRD pattern can be assigned to the β-Bi_2O_3 precursor, with maximum intensity for the (201) reflection.

At pH 8 and 10, the intensity of this Bragg reflection clearly decreases with time during the reaction with the buffer solution. In contrast, the intensities of all Bragg reflections remain almost constant at pH 12, thus indicating that no conversion of the starting material takes place at this pH value. Figure 2 compares the temporal evolution of the normalized (201) intensity of the Bi_2O_3 precursor at pH 8 and 10.

The intensity of the (201) reflection decreases very rapidly at pH 10 and reaches its end offset at around 12.5% of the initial

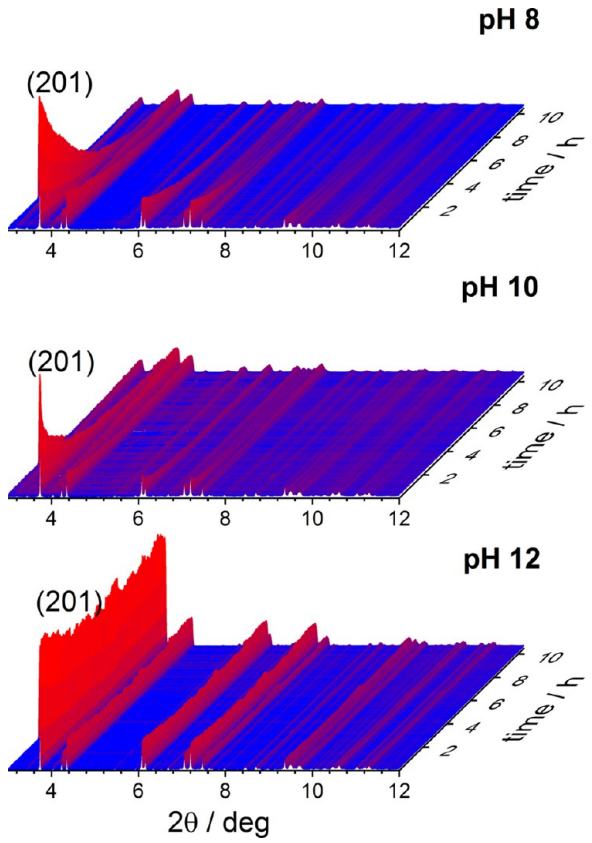

Figure 1. Time-dependent PXRD patterns monitoring the reaction of β-Bi_2O_3 in a $Na_2CO_3/NaHCO_3$ buffer solution at different pH values (top: pH 8, middle: pH 10, and bottom: pH 12).

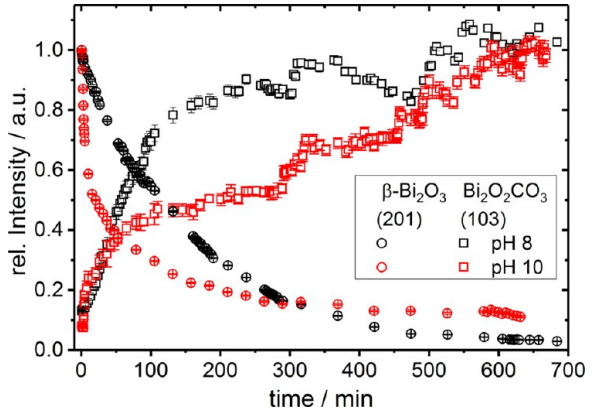

Figure 2. Temporal evolution of the relative intensity of the (201) and (103) Bragg reflections of the β-Bi_2O_3 and $Bi_2O_2CO_3$ phases, respectively, at pH 8 and 10.

intensity. In contrast, we observed an almost ideal monoexponential decay of the normalized (201) intensity with a lifetime of 161 ± 1 min at pH 8 (see Figure S1).

At pH 10, the decay of this Bragg reflection clearly does not exhibit such monoexponential kinetics. Furthermore, we observed a nearly complete conversion of the β-Bi_2O_3 starting material at pH 10. These different decays of the (201) reflection intensity clearly indicate a pH dependence of the reaction mechanism.

Additionally, the growth of additional Bragg reflections assigned to $Bi_2O_2CO_3$[35] was monitored while the reaction proceeded further at pH 8 and 10, respectively. The most

DOI: 10.1021/acsomega.7b01359
ACS Omega 2017, 2, 8213−8221

intense (103) reflection of $Bi_2O_2CO_3$ and the (213) reflection of the $(BiO)_4(OH)_2CO_3$ intermediate display rather close *d*-spacings of 2.948 and 3.0296 Å, respectively.[35]

A full pattern fitting was not taken into account for several reasons. First, a complete crystal structure determination of the intermediate phase $(BiO)_4(OH)_2CO_3$ has not been reported to date. Second, the reflections which are most likely arising from this intermediate are low in intensity and quite broadened. Third, the background intensity is not constant and increases while the reaction proceeds.

At pH 8, the in situ PXRD patterns displayed a minor contribution of the intermediate $(BiO)_4(OH)_2CO_3$ phase, which appeared as a weak reflection during the early stages of the reaction and then as a shoulder of the growing (103) reflection of the $Bi_2O_2CO_3$ product (see Figure 3). Minor

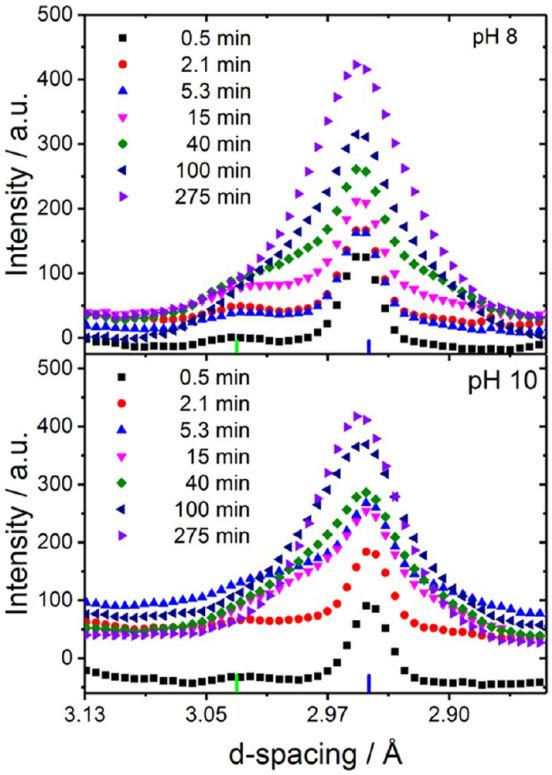

Figure 3. (103) Bragg reflection of $Bi_2O_2CO_3$ for different reaction times (top: pH 8, bottom: pH 10, green vertical bar: (213) reflection of $(BiO)_4(OH)_2CO_3$, blue vertical bar: (103) reflection of $Bi_2O_2CO_3$).

contributions of the hydroxide intermediate can be as well observed at pH 10 (see Figure 3). The temporal evolution of the (103) $Bi_2O_2CO_3$ reflection at pH 8 reveals a sigmoidal growth (see Figure 2), whereas the growth of the (103) reflection at pH 10 follows more complex kinetics. Surprisingly, the intensity of this reflection is still rising after the decay of the (201) β-Bi_2O_3 reflection already reached its end offset. This behavior might be explained by the presence of an amorphous intermediate or by the formation of $Bi_2O_2CO_3$ from solvated Bi^{3+} ions. Both hypotheses are in line with the higher background of the PXRD patterns recorded at pH 10 (see Figure 3). The kinetics of the formation of $Bi_2O_2CO_3$ was evaluated by standard procedures.[36,37] Detailed information on the kinetics of the crystallization process can be obtained by applying the well-known Avrami equation[38−40]

$$\alpha = 1 - e^{-(kt)^n} \quad (4)$$

α represents the value of the extent of reaction at a given time. This value can be calculated from the intensity of a Bragg reflection (*hkl*) according to $\alpha(t) = I_{hkl}(t)/I_{hkl}(t_\infty)$, where $I_{hkl}(t)$ is the intensity of the Bragg reflection at the time *t* and $I_{hkl}(t_\infty)$ represents the final intensity after the reaction has run to completion. *k* represents the rate constant in eq 4, and the exponent *n* is determined to differentiate between different reaction mechanisms.[41] The value of *n* is most easily visualized through Sharp−Hancock plots on the basis of the following expression[42]

$$\ln(-\ln(1-\alpha)) = n\ln(t) + n\ln(k) \quad (5)$$

A linear Sharp−Hancock plot indicates that the reaction mechanism remains unchanged throughout the entire reaction time.

The Sharp−Hancock plots for the (103) reflection of $Bi_2O_2CO_3$ are shown in Figure 4. For the formation process

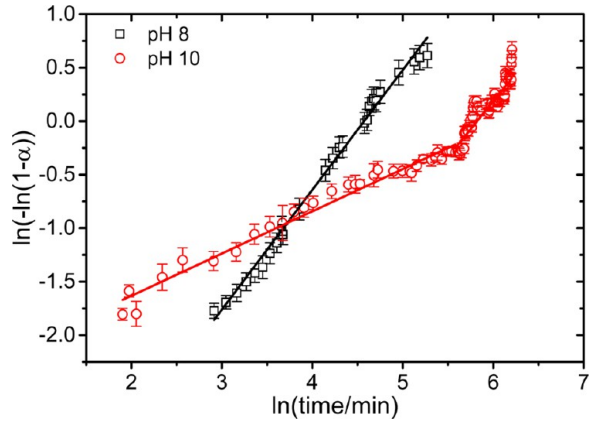

Figure 4. Sharp−Hancock plot for the growth of the (103) Bragg reflection of $Bi_2O_2CO_3$ at pH 8 (black squares) and at pH 10 (red circles) over the range $0.2 < \alpha < 0.85$.

at pH 8, the Sharp−Hancock plot exhibits linear behavior with a slope of 1.12 ± 0.02 over the $0.2 < \alpha < 0.85$ range. These results can be interpreted with the model for a zero-dimensional nucleation, where no diffusion control occurs. In contrast to the zero-dimensional behavior at pH 8, the Sharp−Hancock plot at pH 10 suggests the presence of two mechanisms.

The reaction exponent *n* increases from 0.39 ± 0.01 to 1.04 ± 0.06, thereby indicating an initial diffusion-controlled reaction mechanism up to a reaction time of ∼285 min.

Ex Situ Analysis of $Bi_2O_2CO_3$ Growth. Figure 5 compares representative scanning electron microscopy (SEM) images of the β-Bi_2O_3 precursor and $Bi_2O_2CO_3$ samples obtained at pH 8, 10, and 12. The commercially available β-Bi_2O_3 precursor (Sigma-Aldrich) consists of spherical and sheet-like particles with a diameter of 100−300 nm (Figure 5a). Related irregular morphologies of $Bi_2O_2CO_3$ were obtained after the reactions at pH 8 and 10. In line with the PXRD monitoring (Figure 1), the spherical and sheet-like precursor particles were retained at pH 12.

Fourier transform infrared (FT-IR) and Raman spectroscopy provide additional evidence for the formation of $Bi_2O_2CO_3$ at pH 8 and 10 (see Figure 6). At pH 12, no significant differences

DOI: 10.1021/acsomega.7b01359
ACS Omega 2017, 2, 8213−8221

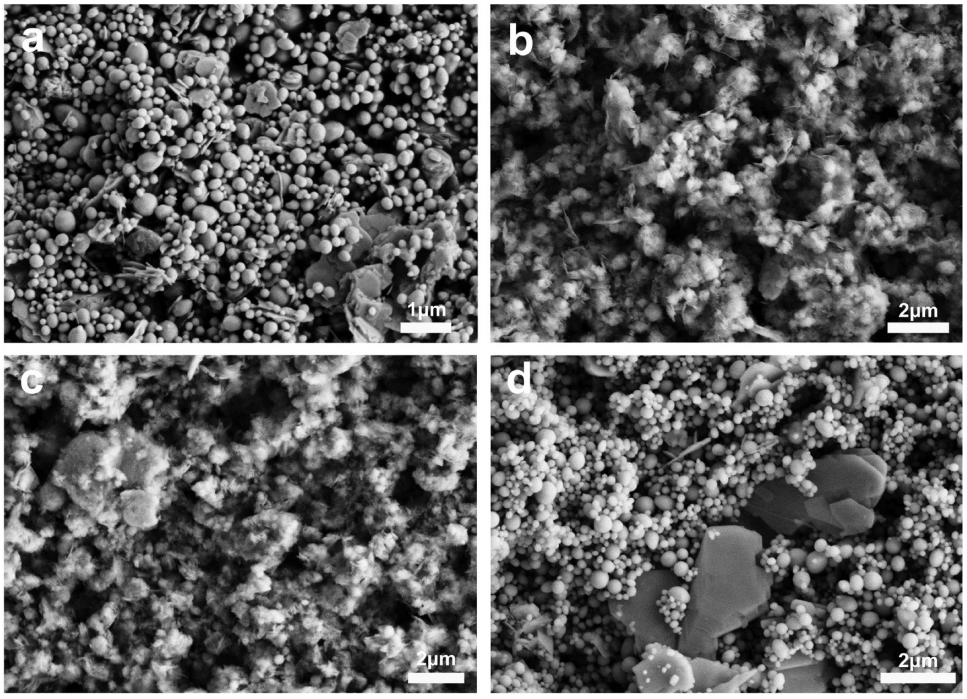

Figure 5. Representative SEM images of (a) Bi_2O_3 (Sigma-Aldrich) and products obtained at different pH values: (b) pH 8, (c) pH 10, and (d) pH 12.

between the spectra of the precursor and of a representative sample obtained after 10 h reaction time can be observed.

In particular, the Raman spectrum of the sample after treatment with carbonate buffer at pH 12 is virtually identical to the precursor spectrum. This corresponds to the results from in situ PXRD and ex situ SEM which both point to a reaction parameter window between pH 8 and 10 for $Bi_2O_2CO_3$ formation.

The FT-IR spectra of reaction products at pH 8 and 10 show a clear intensity increase of the out-of-plane bending vibration of the carbonate anion at 845 cm^{-1}, thereby corroborating the CO_2 uptake process during the reaction.[35,43] Raman spectra of samples obtained at pH 8 and 10 display the growth of new bands in the spectral region 840−1100 cm^{-1}, which can be assigned to the normal modes of the CO_3^{2-}. The most intense Raman band at 1067 cm^{-1} corresponds to the symmetric carbonate stretch motion.[35,43]

Quenching experiments were performed using the same experimental conditions as those for the synchrotron experiments to correlate the pH dependency and kinetic trends emerging from the in situ X-ray diffraction (XRD) monitoring with the parameter window for $Bi_2O_2CO_3$ formation under ex situ conditions.

A summary evaluation of the PXRD patterns obtained from quenching the reaction after different durations (0.5−12 h) at different pH values (8, 9, 10, 11, and 12) can be found in Table S3. The quenching resulted in similar PXRD patterns for samples obtained in the pH range 8−11 (see Figure S2). The starting material (β-Bi_2O_3) was gradually converted into $Bi_2O_2CO_3$. The evaluation of the educt/product ratio through PXRD refinement after 0.5 and 4 h at pH 10 showed that only 30 and 7% of the educt remained, respectively. This appears considerably faster when compared with the values obtained from the in situ measurements (Figure 1, 50 and 20%, respectively). However, a direct comparison between these values remains difficult because the continuation of the reaction

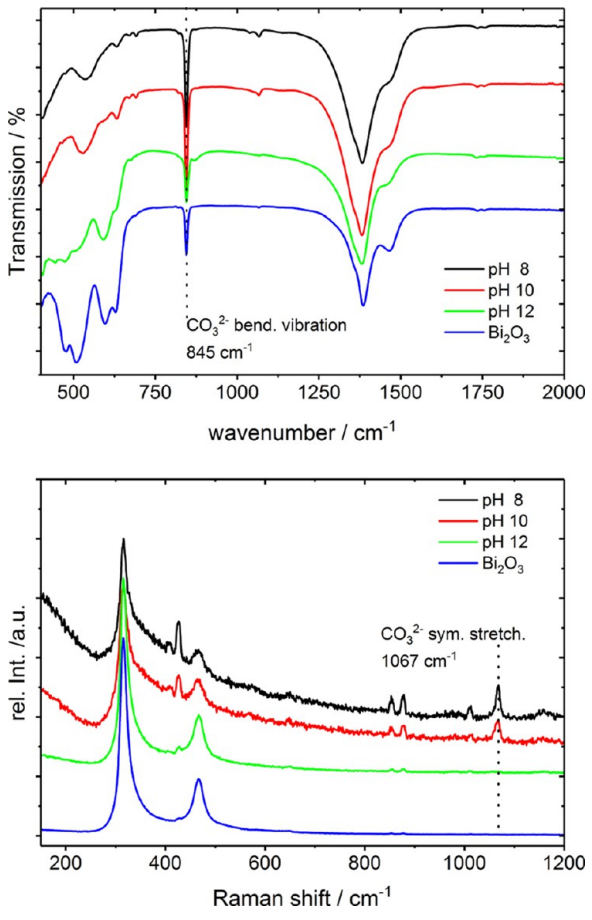

Figure 6. FT-IR (top) and Raman (bottom) spectra of products obtained at different pH values after 10 h vs β-Bi_2O_3 precursor.

DOI: 10.1021/acsomega.7b01359
ACS Omega 2017, 2, 8213−8221

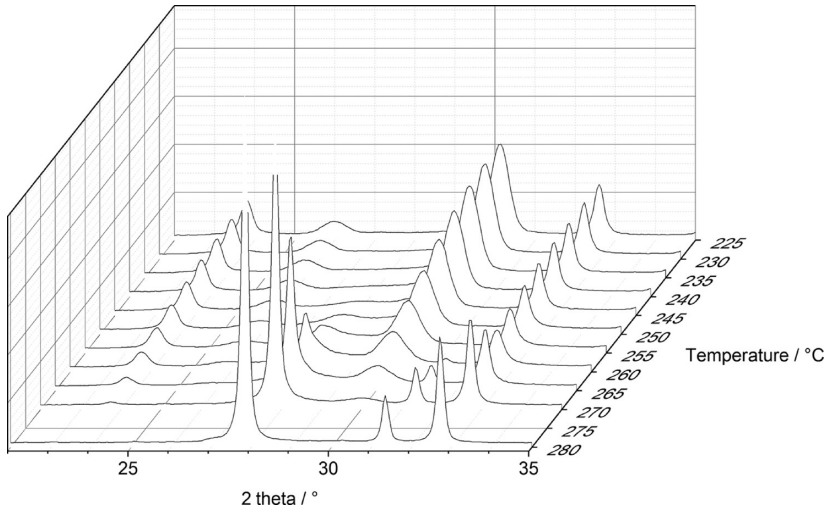

Figure 7. HT-PXRD monitoring between 225 and 280 °C showing the decomposition of $Bi_2O_2CO_3$ to β-Bi_2O_3 (cf. also Figure S6).

Table 1. Overview of $\beta \rightarrow \alpha$ Phase Transformation Sequences for Different Starting Materials

sample	origin/synthesis	T/°C onset ($\beta \rightarrow \alpha$)	phase purity (XRD)	SEM	BET/m^2 g^{-1}
β-Bi_2O_3(a)	Aldrich (99.8%)	260	pure	nanospheres (100 nm diameter); Scherrer equation: ca. 60 nm	3
β-Bi_2O_3(b)	decomposition of $Bi_2O_2CO_3$ at 300 °C $Bi_2O_2CO_3$ synthesized according to ref 11 using $Bi(NO_3)_3$ (Aldrich, 98%)	320−340	pure	microspheres (1−2 μm diameter) of agglomerated particles; Scherrer equation: ca. 78 nm	3
β-Bi_2O_3(c)	same as above $Bi(NO_3)_3$ (Aldrich, 99.999%) and Milli-Q water were used instead	>300	$Bi_2O_2CO_3$ impurities	see Figure S10	16
β-Bi_2O_3(d)	decomposition of $Bi_2O_2CO_3$ at 300 °C $Bi_2O_2CO_3$ synthesized by reaction of β-Bi_2O_3 (Aldrich, 99.8%) with Na_2CO_3/$NaHCO_3$ buffer solution (0.1 M) in Milli-Q water	>300	pure	see Figure S10	6−7
$Bi_2O_2CO_3$	$Bi_2O_2CO_3$ synthesized according to ref 11 using $Bi(NO_3)_3$ (Aldrich, 98%)	320−340	HT-XRD		

with atmospheric CO_2 and humidity after quenching cannot totally be excluded. At pH 12, the ex situ reaction behavior changes drastically. The reflections of the starting material dominate the patterns from start to finish (see Figure S3), and only traces of $Bi_2O_2CO_3$ can be observed. These findings are in good agreement with the present in situ results. Additionally, small amounts of $(BiO)_4(OH)_2CO_3$ are formed at pH 12. Interestingly, only $(BiO)_4(OH)_2CO_3$ was formed after a further pH increase to 13.

When comparing the notably different time scales for $Bi_2O_2CO_3$ formation under in situ and ex situ conditions with identical amounts of starting material and reaction containers, a possible influence of 60 keV in situ X-ray irradiation on the nucleation process might also be taken into account.[44,45]

Influence of the Preparative History on Bismuth Oxide Phase Transformations. To assess the potential of room-temperature-synthesized $Bi_2O_2CO_3$ for targeted access to selective Bi_2O_3 modifications or to Bi_2O_3/$Bi_2O_2CO_3$ heterojunctions, its thermal decomposition behavior was studied with several methods. For this purpose, phase pure $Bi_2O_2CO_3$ was synthesized according to literature procedures to exclude any precursor traces.[11]

First, thermogravimetric analysis (TGA) data (see Figure S4) showed the decomposition of $Bi_2O_2CO_3$ to Bi_2O_3 above 300 °C, in line with earlier reports.[35,43] The temperature interval for the conversion of $Bi_2O_2CO_3$ into α- or β-Bi_2O_3, respectively, was first narrowed down with ex situ thermal decomposition experiments through heat treatment under ambient conditions in the range of 240−340 °C (Table S4). Decomposition of $Bi_2O_2CO_3$ to β-Bi_2O_3 proceeds between 240 and 260 °C, followed by transformation into α-Bi_2O_3 between 300 and 320 °C. This temperature window was then compared to the β- to α-phase transformation temperature range for commercially available β-Bi_2O_3. Interestingly, the phase change of the commercially purchased starting material was observed at a significantly lower temperature, namely around 260 °C (Table S4).

To substantiate these ex situ results, both home-made $Bi_2O_2CO_3$ and commercial β-Bi_2O_3 were subjected to high-temperature powder X-ray diffraction (HT-PXRD) monitoring. PXRD patterns were recorded every 5 °C after a holding time of 30 min at a constant temperature in air.

Decomposition of $Bi_2O_2CO_3$ (Figure 7) was observed at around 260 °C in good agreement with the above ex situ measurements. Likewise, the subsequent transformation of β- to α-Bi_2O_3 (Figure S6) took place at a similar temperature interval as recorded ex situ (320−340 °C), and traces of the α-phase could already be observed at 325 °C.

Next, the unexpectedly low transformation temperature of commercially available β-Bi_2O_3 (**β-Bi_2O_3(a)**, Table 1) was confirmed by high-temperature X-ray diffraction (HT-XRD)

DOI: 10.1021/acsomega.7b01359
ACS Omega 2017, 2, 8213−8221

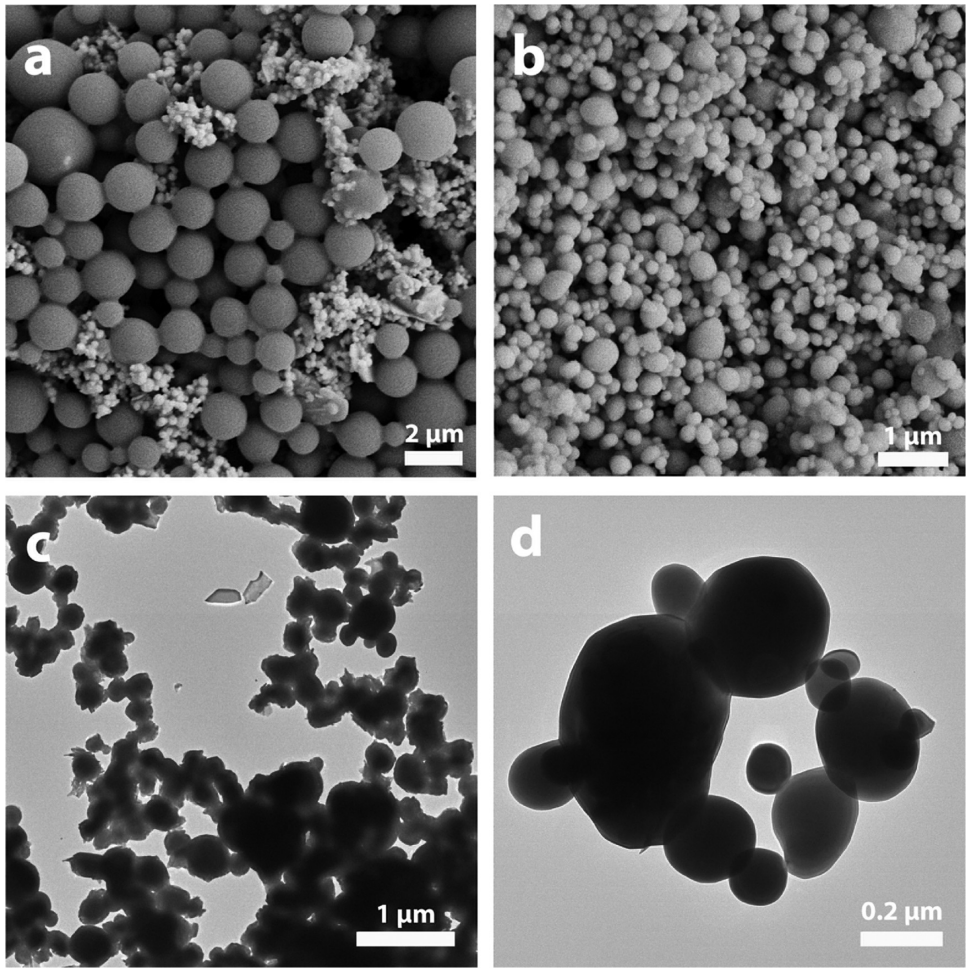

Figure 8. (a) Representative SEM image of as-synthesized β-Bi_2O_3(b) (from $Bi(NO_3)_3$ precursor, material coated with 10 nm Pt), (b) SEM image of commercially available β-Bi_2O_3(a) (material coated with 10 nm Pt), (c) TEM image of as-synthesized β-Bi_2O_3(b) (from $Bi(NO_3)_3$ precursor), and (d) TEM image of commercially available β-Bi_2O_3(a).

measurements. First reflections of α-Bi_2O_3 indeed appeared at 260 °C. Their intensity increased constantly with temperature until completely phase pure α-Bi_2O_3 was obtained at 290 °C (Figure S7).

Previous works established links between the particle size of bismuth oxide nanomaterials and their respective phase diagrams.[27,46,47] To further investigate the influence of preparative history and particle size on the notably different β- to α-transformation points of the two Bi_2O_3 source materials, we isolated phase pure β-Bi_2O_3 (PXRD in Figure S8) through decomposition of $Bi_2O_2CO_3$ at 300 °C (β-Bi_2O_3(b), Table 1). Here, the phase change to α-Bi_2O_3 occurred after heat treatment at 320−340 °C.

Surprisingly, it was not possible to monitor the phase transformation of commercial β-Bi_2O_3 to α-Bi_2O_3 with differential thermal analysis (DTA) methods although a wide range of heating rates was applied (1−10 K/min in argon and air). The transformation enthalpy of the phase transition has been reported within a range between −9 and −4 kJ/mol, which is rather low and can easily be overlooked in a DTA measurement.[26,48]

The particle sizes and morphologies of as-synthesized β-Bi_2O_3(b−d) and commercially available β-Bi_2O_3(a) were investigated with SEM, transmission electron microscopy (TEM), Brunauer−Emmett−Teller (BET), and Scherrer-equation analysis (see Figures 8, S10, and Table 1). On the basis of the Scherrer-equation analysis using the full width at half-maximum of the (201) main reflection, we estimated a crystallite size for β-Bi_2O_3(a) and the as-synthesized β-Bi_2O_3(b) of 78 ± 2 and 60 ± 1 nm, respectively.[49] BET measurements also show closely related specific surface areas of 3 m^2/g for both samples. SEM images of as-synthesized β-Bi_2O_3(b) and commercially available β-Bi_2O_3(a) are compared in Figure 8. SEM images of as-synthesized β-Bi_2O_3(b) show microspheres ranging from 1 to 3 μm diameter together with some smaller spheres that are strongly agglomerated. However, TEM images of as-synthesized β-Bi_2O_3(b) show particles with smaller sizes. On the basis of SEM and TEM results, commercially available β-Bi_2O_3(a) consists of nanospheres with diameters of 100−200 nm. Table 1 provides a summary of the characterization and phase transformation behavior of all starting materials investigated in the present study.

In summary, despite SEM results showing microspheres for the as-synthesized β-Bi_2O_3, PXRD evidence does not indicate significant differences in the crystallite size of the as-synthesized sample β-Bi_2O_3(b) and commercially available β-Bi_2O_3(a). The observed discrepancy in the SEM results can be due to agglomeration, which is also visible in the TEM images (see Figure 8). The grain boundaries expected in the SEM images of β-Bi_2O_3(b) are probably concealed by the 10 nm Pt layer

DOI: 10.1021/acsomega.7b01359
ACS Omega 2017, 2, 8213−8221

applied during sample preparation. Therefore, we assume that the significantly lower phase transition temperature for the $\beta \rightarrow \alpha$ transition of $\boldsymbol{\beta}$-$\mathbf{Bi_2O_3}$(**a**) is most likely not a size effect.

Therefore, additional experiments were conducted with ultrapure starting materials to exclude possible influences of impurities on the $\beta \rightarrow \alpha$ transition temperature. For this purpose, the $Bi_2O_2CO_3$ precursor was prepared via two different routes, namely either by reaction of commercial β-Bi_2O_3 in Na_2CO_3/$NaHCO_3$ buffer solution over night or by the coprecipitation method with $Bi(NO_3)_3$ and Na_2CO_3 as starting materials. Both synthesis routes yielded phase pure $Bi_2O_2CO_3$. All materials were placed in the same muffle furnace and heated to 300 °C for 2 h vs commercial $\boldsymbol{\beta}$-$\mathbf{Bi_2O_3}$(**a**) as a reference. PXRD measurements of the three samples were conducted after cooling down to room temperature. The two $Bi_2O_2CO_3$ samples obtained by different synthesis routes both yielded β-Bi_2O_3 after heat treatment, whereas α-Bi_2O_3 was obtained from commercial $\boldsymbol{\beta}$-$\mathbf{Bi_2O_3}$(**a**).

In summary, all β-Bi_2O_3 samples (**b**−**d**) synthesized using carbonate salts afforded materials with higher $\beta \rightarrow \alpha$ phase transformation temperatures compared with commercially available $\boldsymbol{\beta}$-$\mathbf{Bi_2O_3}$(**a**) (Table 1). This phenomenon might be linked to the presence of stabilizing carbonate groups on the surface of the respective β-Bi_2O_3 samples along the lines of previous studies.[27] Attempts to synthesize β-Bi_2O_3 via a carbonate-free route did not work and only resulted in the direct formation of phase pure α-Bi_2O_3 instead.[50] Given that the analytical characterizations (Table 1) show neither drastic differences in the particle sizes nor an indication for a significant role of impurities, the low $\beta \rightarrow \alpha$ phase transformation temperature for the commercially available $\boldsymbol{\beta}$-$\mathbf{Bi_2O_3}$(**a**) can be due to the absence of a protective carbonate surface layer.

To test this hypothesis, X-ray photoelectron spectroscopy (XPS) measurements were performed to further investigate the surface composition of β-Bi_2O_3 powders from different sources (**a**, **b**) compared to that of two reference samples, namely Na_2CO_3 and $Bi_2O_2CO_3$. Measurements of the C 1s core level emissions give insight into the relative amount of carbonates present at the surface of the samples (Figure S11a). All investigated samples show peaks from adventitious carbon that are commonly observed in ex situ XPS measurements. In addition to these adsorbate emissions, strong carbonate peaks are visible for the two reference samples. In combination with the analysis of the O 1s core level emission (Figure S11b), this unambiguously confirms the presence of carbonates in these samples. For both the $\boldsymbol{\beta}$-$\mathbf{Bi_2O_3}$(**a**) and $\boldsymbol{\beta}$-$\mathbf{Bi_2O_3}$(**b**) samples, the carbonate components in both C 1s and O 1s spectra are much less pronounced. This renders the presence of a dense protective carbonate surface shell unlikely, and only a thin surface layer may be present. However, given the qualitative nature of the results and the low relative intensity of the carbonate emissions, no straightforward connection between carbonate groups on the surface and the different phase transition temperatures can be made.

The Bi_2O_3 materials after different treatments (Table 1) were stored in vials in air after all analytics had been conducted. After a few weeks, we observed a color bleaching from bright yellow (β-Bi_2O_3) to light beige. Additional PXRD measurements were performed that showed that substantial amounts of $Bi_2O_2CO_3$ were now present in the previously phase pure β-Bi_2O_3 materials. We concluded that the β-Bi_2O_3 had reacted with ambient carbon dioxide during storage to form $Bi_2O_2CO_3$. This may arise from residual $Bi_2O_2CO_3$ precursor amounts acting as seed crystals. To check whether the formation of $Bi_2O_2CO_3$ could be accelerated, we conducted the following reference experiment. As-synthesized $\boldsymbol{\beta}$-$\mathbf{Bi_2O_3}$(**b**) was exposed to a controlled CO_2 rich gas flow (10 mL/min CO_2 in argon) at 30 °C for 60 h in the TGA device. The presence of $Bi_2O_2CO_3$ after such treatment was confirmed by PXRD measurement (31% according to Rietveld analysis, Figure S12). Commercially available $\boldsymbol{\beta}$-$\mathbf{Bi_2O_3}$(**a**) was exposed to an analogous CO_2 gas flow under identical conditions, but no formation of $Bi_2O_2CO_3$ was detected in subsequent PXRD measurements (Figure S12). Because the commercial material also showed surface carbonate peaks in the XPS measurements, the presumed carbonate seed crystals are most likely not the sole reason for the carbonate formation. Further investigations beyond the scope of this study are required to fully understand the complex parameter dependence of the observed phase transitions.

All in all, the significant influence of manifold parameters during the preparative history is crucial for the targeted phase selective fabrication of Bi_2O_3/$Bi_2O_2CO_3$ heterojunctions and bismuth oxide materials for different catalytic applications.

CONCLUSIONS

The combination of in situ PXRD with SEM and vibrational spectroscopy studies provided deeper insight into the reaction mechanisms of the room-temperature formation of $Bi_2O_2CO_3$ as an attractive multifunctional material for CO_2 capture and photocatalysis. The formation mechanisms of $Bi_2O_2CO_3$ show pronounced pH dependence, with a reaction window between pH 8 and 10. Time-resolved X-ray diffraction monitoring clearly indicates that $Bi_2O_2CO_3$ is formed via different pathways at pH 8 and 10, respectively. At pH 8, a stronger contribution of the $(BiO)_4(OH)_2CO_3$ intermediate phase goes hand in hand with a higher extent of precursor conversion. Sharp−Hancock plots can be interpreted with a zero-dimensional nucleation model for $Bi_2O_2CO_3$ growth at pH 8. This scenario is changed at pH 10: up to a reaction time of ∼285 min, the nucleation process is in line with a diffusion-controlled model, which then turns toward zero-dimensional nucleation kinetics. Ex situ quenching experiments confirmed these trends, albeit with different $Bi_2O_2CO_3$ formation kinetics compared with in situ monitoring. The present results indicate that important main trends for formation parameter windows can be derived from in situ monitoring, which open up new options for optimizing the production and performance of economic $Bi_2O_2CO_3$ catalysts for environmental applications. Subsequent conversion experiments on the $\beta \rightarrow \alpha$ phase transformation temperature of bismuth oxide samples from different sources indicate a major influence of the synthetic protocol. Samples obtained from carbonate-based starting materials displayed higher transition temperatures to α-Bi_2O_3 than to commercially available β-Bi_2O_3 with comparable crystallite size and surface area. Follow-up studies are under way to fully establish the detailed pH specific growth mechanisms. Investigations into the role of protective carbonate surface layers are expected to exploit the preprative history of bismuth oxide-related precursors as a key parameter for their targeted transformation into phase pure functional materials, such as catalytically active heterojunctions.

EXPERIMENTAL SECTION

The time-resolved PXRD experiments were performed at the P02 beamline of the PETRA III storage ring at HASYLAB.[51,52]

DOI: 10.1021/acsomega.7b01359
ACS Omega 2017, 2, 8213−8221

The beamline is operated at a fixed energy of 60 keV with a relative energy bandwidth $\Delta E/E$ of 10^{-4}.[51] β-Bi_2O_3 (20 mg, 42.9 μmol, Sigma-Aldrich, 99.8%, PXRD in Figure S8) was dispersed in 2 mL of Na_2CO_3/$NaHCO_3$ buffer solution (100 mM, pH 10) and stirred during the reaction. For the other measurement series, the pH of the buffer solution was adjusted to 8 and 12 by adding diluted solutions of HCl and NaOH, respectively. Reactions were performed in sodium carbonate buffer to mimic a high CO_2 partial pressure and to control the pH of the reaction medium. The applied CO_2 concentration is significantly higher compared to the saturation concentration at atmospheric partial pressure ($c = H^{cp} \cdot pCO_2 = 3.34 \times 10^{-2}$ M/atm $\times$ 3.9×10^{-4} atm = 0.013 mM; H^{cp} = Henry constant).[53] All samples were placed in polypropylene screw cap tubes for synchrotron experiments (TPP Techno Plastic Products AG, ø 12 mm).

Room-temperature in situ PXRD patterns were recorded every 30 s using a fast two-dimensional detector (PerkinElmer XRD1621) at a wavelength of 0.20751 Å. Background subtraction and radial integration of the PXRD pattern were performed with the Fit2D software.[54] For background subtraction, an XRD pattern of a sample container filled only with buffer solution was recorded and this image was subtracted prior to radial integration. CeO_2 was used as a calibration standard for the determination of the beam center. Ex situ FT-IR and Raman spectra were recorded on a Bruker VERTEX 70 spectrometer with a platinum attenuated total reflection accessory and on a Renishaw Ramascope spectrometer equipped with a diode laser (785 nm), respectively. Scanning electron microscopy images were recorded on a SEM Zeiss Supra 50 VP. Prior to measurements, the samples were coated with 10 nm of Pt. Phase pure $Bi_2O_2CO_3$ was obtained from a literature procedure.[11] TEM investigations were performed with a FEI Talos F200X (200 kV) high-resolution transmission electron microscope. Samples were deposited on the 300 mesh copper grid before measurement.

Ex situ room-temperature XRD patterns were recorded on a STOE STADI P diffractometer in transmission mode (flat-plate sample holder, Ge monochromator, and Cu Kα_1 radiation) using a position-sensitive microstrip solid-state detector (MYTHEN 1 K). Temperature-dependent PXRD data on phase pure $Bi_2O_2CO_3$ were obtained with a Panalytical X'Pert PRO MPD using a high-temperature furnace. Cu Kα radiation (1.541874 Å) was generated under 45 kV and 40 mA, sent through a 0.04 rad soller slit, a $\frac{1}{8}$ divergence slit and a 10 mm wide beam mask to irradiate the sample. The diffracted beams were collected using an X'Celerator RTMS detector equipped with a 5 mm antiscatter and a Ni Kβ-filter. All powder samples were placed on alumina sample holders that were mounted on a height control stage for micrometer-precise sample height alignment. Prior to measurements, the sample was centered within the beam by adjusting the sample holder height so that the initial intensity was reduced by ~50%. All measurements were performed under atmospheric conditions (in air). The temperature-programmed PXRD experiments were conducted under the following protocol. The first PXRD pattern was recorded at room temperature prior to any thermal treatment. Subsequently, the sample was heated to the desired temperatures (max 400 °C) using a rate of 2 K/min. Then, the temperature was held for further 30 min to ensure thermal equilibration and the completion of chemical processes before recording a powder diffractogram in 5 K intervals. After reaching the final temperature, the sample was allowed to cool down to room temperature and then another pattern was recorded. Thermogravimetric analysis (TGA) of the samples was conducted using a Netzsch Jupiter STA 449 F3 TGA in inert atmosphere (argon).

X-ray photoelectron spectroscopy (XPS) was conducted on selected samples using a Physical Electronics Quantum 2000 X-ray photoelectron spectrometer featuring monochromatic Al Kα radiation, generated from an electron beam operated at 15 kV and 32.3 W. The energy scale of the instrument was calibrated using Au and Cu reference samples. The samples were firmly pressed onto indium foil patches, which were then mounted onto a sample plate and introduced into the spectrometer. The analysis was conducted at 1×10^{-6} Pa, with an electron take off angle of 45° and a pass energy of 23.50 eV for all samples. Charge compensation during the measurement was achieved using a low-energy electron source. The acquired spectra were then aligned using the C−C component of the C 1s core level emission at 284.5 eV.

■ ASSOCIATED CONTENT

Supporting Information

The Supporting Information is available free of charge on the ACS Publications website at DOI: 10.1021/acsomega.7b01359.

Additional ex situ/in situ PXRD patterns; SEM investigations; XPS results; and TGA/DTA measurements (PDF)

■ AUTHOR INFORMATION

Corresponding Author

*E-mail: greta.patzke@chem.uzh.ch.

ORCID

Ying Zhou: 0000-0001-9995-0652

Greta R. Patzke: 0000-0003-4616-7183

Author Contributions

⊥R.M. and M.O. contributed equally to this work.

Notes

The authors declare no competing financial interest.

■ ACKNOWLEDGMENTS

This work was supported by Swiss National Science Foundation (Sinergia Grant No. CRSII2_160801/1) and by the University Research Priority Program "Light to Chemical Energy Conversion" (URPP LightChEC). Ying Zhou acknowledges financial support from the National Natural Science Foundation of China (U1232119). Sebastian Siol acknowledges funding from the COST project IZCNZ0-174856 C16.0075, in the COST Action MP1407 (e-MINDS). The authors thank Jana Michalikova (HASYLAB) for support during the beamtime.

■ REFERENCES

(1) Meng, X.; Zhang, Z. *J. Mol. Catal. A: Chem.* **2016**, *423*, 533−549.

(2) Madhusudan, P.; Zhang, J.; Cheng, B.; Liu, G. *CrystEngComm* **2013**, *15*, 231−240.

(3) Cao, F.; Wang, J.; Tu, W.; Lv, X.; Li, S.; Qin, G. *Funct. Mater. Lett.* **2015**, *8*, No. 1550021.

(4) Huang, H.; Wang, J.; Dong, F.; Guo, Y.; Tian, N.; Zhang, Y.; Zhang, T. *Cryst. Growth Des.* **2015**, *15*, 534−537.

(5) Song, P.-Y.; Xu, M.; Zhang, W.-D. *Mater. Res. Bull.* **2015**, *62*, 88−95.

DOI: 10.1021/acsomega.7b01359
ACS Omega 2017, 2, 8213−8221

(6) Ni, Z.; Sun, Y.; Zhang, Y.; Dong, F. *Appl. Surf. Sci.* **2016**, *365*, 314−335.
(7) Zhou, Y.; Wang, H.; Sheng, M.; Zhang, Q.; Zhao, Z.; Lin, Y.; Liu, H.; Patzke, G. R. *Sens. Actuators, B* **2013**, *188*, 1312−1318.
(8) Zai, J.; Cao, F.; Liang, N.; Yu, K.; Tian, Y.; Sun, H.; Qian, X. *J. Hazard. Mater.* **2017**, *321*, 464−472.
(9) Wang, Z.; Huang, Y.; Ho, W.; Cao, J.; Shen, Z.; Lee, S. C. *Appl. Catal., B* **2016**, *199*, 123−133.
(10) Hu, R.; Xiao, X.; Tu, S.; Zuo, X.; Nan, J. *Appl. Catal., B* **2015**, *163*, 510−519.
(11) Cheng, H.; Huang, B.; Yang, K.; Wang, Z.; Qin, X.; Zhang, X.; Dai, Y. *ChemPhysChem* **2010**, *11*, 2167−2173.
(12) Wang, Q.; Zheng, L.; Chen, Y.; Fan, J.; Huang, H.; Su, B. *J. Alloys Compd.* **2015**, *637*, 127−132.
(13) Dong, F.; Ho, W.-K.; Lee, S. C.; Wu, Z.; Fu, M.; Zou, S.; Huang, Y. *J. Mater. Chem.* **2011**, *21*, 12428−12436.
(14) Cen, W.; Xiong, T.; Tang, C.; Yuan, S.; Dong, F. *Ind. Eng. Chem. Res.* **2014**, *53*, 15002−15011.
(15) Zhao, T.; Zai, J.; Xu, M.; Zou, Q.; Su, Y.; Wang, K.; Qian, X. *CrystEngComm* **2011**, *13*, 4010−4017.
(16) Zheng, Y.; Duan, F.; Chen, M.; Xie, Y. *J. Mol. Catal. A: Chem.* **2010**, *317*, 34−40.
(17) Huang, H.; Tian, N.; Jin, S.; Zhang, Y.; Wang, S. *Solid State Sci.* **2014**, *30*, 1−5.
(18) Chen, R.; So, M. H.; Yang, J.; Deng, F.; Che, C.-M.; Sun, H. *Chem. Commun.* **2006**, 2265−2267.
(19) Liu, H.; Patzke, G. R. *Chem. - Asian J.* **2014**, *9*, 2249−2259.
(20) Schulze, A. S.; Tavernaro, I.; Machka, F.; Dakischew, O.; Lips, K. S.; Wickleder, M. S. *J. Nanopart. Res.* **2017**, *19*, No. 70.
(21) Liang, N.; Wang, M.; Jin, L.; Huang, S.; Chen, W.; Xu, M.; He, Q.; Zai, J.; Fang, N.; Qian, X. *ACS Appl. Mater. Interfaces* **2014**, *6*, 11698−11705.
(22) Hu, R.; Xiao, X.; Tu, S.; Zuo, X.; Nan, J. *Appl. Catal., B* **2015**, *163*, 510−519.
(23) Zhu, G.; Liu, Y.; Hojamberdiev, M.; Han, J.; Rodríguez, J.; Bilmes, S. A.; Liu, P. *New J. Chem.* **2015**, *39*, 9557−9568.
(24) Iyyapushpam, S.; Nishanthi, S. T.; Padiyan, D. P. *J. Phys. Chem. Solids* **2015**, *81*, 74−78.
(25) Yu, C.; Zhou, W.; Zhu, L.; Li, G.; Yang, K.; Jin, R. *Appl. Catal., B* **2016**, *184*, 1−11.
(26) Greaves, C.; Blower, S. K. *Mater. Res. Bull.* **1988**, *23*, 1001−1008.
(27) Guenther, G.; Guillon, O. *J. Mater. Res.* **2014**, *29*, 1383−1392.
(28) Pienack, N.; Ruiz Arana, L.; Bensch, W.; Terraschke, H. *Crystals* **2016**, *6*, 157.
(29) Pienack, N.; Bensch, W. *Angew. Chem., Int. Ed.* **2011**, *50*, 2014−2034.
(30) Ibrahimkutty, S.; Wagener, P.; dos Santos Rolo, T.; Karpov, D.; Menzel, A.; Baumbach, T.; Barcikowski, S.; Plech, A. *Sci. Rep.* **2015**, *5*, No. 16313.
(31) Letzel, A.; Gökce, B.; Wagener, P.; Ibrahimkutty, S.; Menzel, A.; Plech, A.; Barcikowski, S. *J. Phys. Chem. C* **2017**, *121*, 5356−5365.
(32) Wu, Y.; Breeze, M. I.; Clarkson, G. J.; Millange, F.; O'Hare, D.; Walton, R. I. *Angew. Chem., Int. Ed.* **2016**, *55*, 4992−4996.
(33) Chiu, H. W.; Chervin, C. N.; Kauzlarich, S. M. *Chem. Mater.* **2005**, *17*, 4858−4864.
(34) Cook, D. S.; Wu, Y.; Lienau, K.; Moré, R.; Kashtiban, R. J.; Magdysyuk, O. V.; Patzke, G. R.; Walton, R. I. *Chem. Mater.* **2017**, *29*, 5053−5057.
(35) Taylor, P.; Sunder, S.; Lopata, V. J. *Can. J. Chem.* **1984**, *62*, 2863−2873.
(36) Wendt, M.; Mahnke, L. K.; Heidenreich, N.; Bensch, W. *Eur. J. Inorg. Chem.* **2016**, *2016*, 5393−5398.
(37) Zhou, Y.; Antonova, E.; Bensch, W.; Patzke, G. R. *Nanoscale* **2010**, *2*, 2412−2417.
(38) Avrami, M. *J. Chem. Phys.* **1939**, *7*, 1103−1112.
(39) Avrami, M. *J. Chem. Phys.* **1940**, *8*, 212−224.
(40) Avrami, M. *J. Chem. Phys.* **1941**, *9*, 177−184.
(41) Hulbert, S. F. *J. Br. Ceram. Soc.* **1969**, *6*, 11−20.
(42) Hancock, J. D.; Sharp, J. H. *J. Am. Ceram. Soc.* **1972**, *55*, 74−77.
(43) Tobon-Zapata, G. E.; Etcheverry, S. B.; Baran, E. J. *J. Mater. Sci. Lett.* **1997**, *16*, 656−657.
(44) Martis, V.; Nikitenko, S.; Sen, S.; Sankar, G.; van Beek, W.; Filinchuk, Y.; Snigireva, I.; Bras, W. *Cryst. Growth Des.* **2011**, *11*, 2858−2865.
(45) Feldman, Y.; Lyahovitskaya, V.; Leitus, G.; Lubomirsky, I.; Wachtel, E.; Bushuev, V. A.; Vaughan, G.; Barkay, Z.; Rosenberg, Y. *Appl. Phys. Lett.* **2009**, *95*, No. 051919.
(46) Guenther, G.; Theissmann, R.; Guillon, O. *J. Phys. Chem. C* **2014**, *118*, 27020−27027.
(47) Guenther, G.; Kruis, F. E.; Guillon, O. *J. Phys. Chem. C* **2014**, *118*, 27010−27019.
(48) Rao, C. N. R.; Subba Rao, G. V.; Ramdas, S. *J. Phys. Chem.* **1969**, *73*, 672−675.
(49) Gashti, M. P.; Stir, M.; Hulliger, J. *New J. Chem.* **2016**, *40*, 5495−5500.
(50) Lu, Y.; Zhao, Y.; Zhao, J.; Song, Y.; Huang, Z.; Gao, F.; Li, N.; Li, Y. *Cryst. Growth Des.* **2015**, *15*, 1031−1042.
(51) Dippel, A.-C.; Liermann, H.-P.; Delitz, J. T.; Walter, P.; Schulte-Schrepping, H.; Seeck, O. H.; Franz, H. *J. Synchrotron Radiat.* **2015**, *22*, 675−687.
(52) Liermann, H.-P.; Morgenroth, W.; Ehnes, A.; Berghäuser, A.; Winkler, B.; Franz, H.; Weckert, E. *J. Phys.: Conf. Ser.* **2010**, *215*, No. 012029.
(53) Sander, R. *Atmos. Chem. Phys.* **2015**, *15*, 4399−4981.
(54) Hammersley, A. P.*Fit2D Program Package*, v5.18, 1995.

DOI: 10.1021/acsomega.7b01359
ACS Omega 2017, 2, 8213−8221